

**STUDY OF MAGNETIC MOTIONS IN THE SOLAR PHOTOSPHERE  
AND THEIR IMPLICATIONS FOR HEATING THE SOLAR ATMOSPHERE**

NASA Grant NAGW-2545

IN-92-OR  
167142

Final Report

For the period 1 June 1991 through 30 September 1997

Principal Investigator

Robert W. Noyes

May 1998

Prepared for

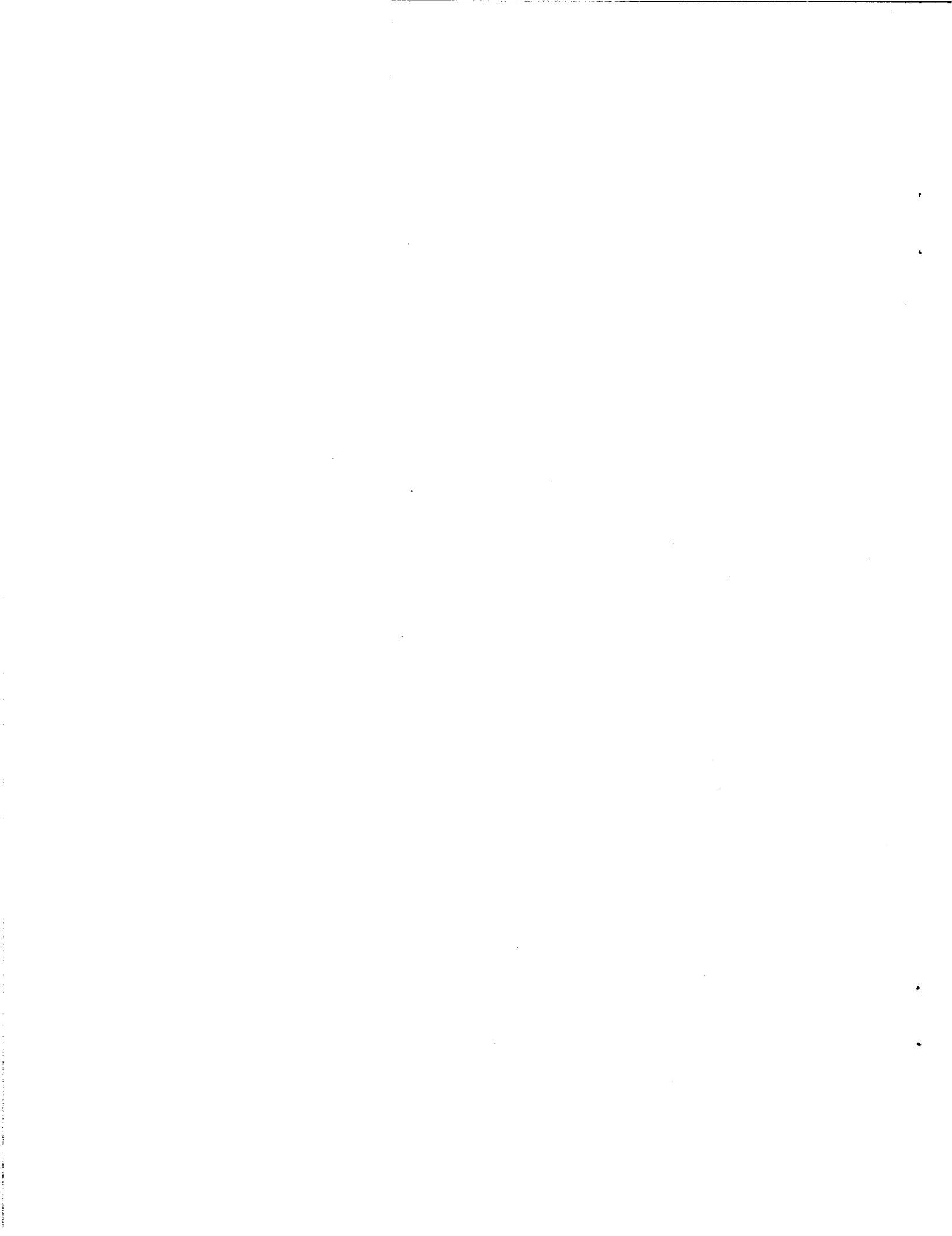
National Aeronautics and Space Administration

Washington, D.C. 20546

Smithsonian Institution  
Astrophysical Observatory  
Cambridge, Massachusetts 02138

The Smithsonian Astrophysical Observatory  
is a member of the  
Harvard-Smithsonian Center for Astrophysics

The NASA Technical Officer for this Grant is Dr. William J. Wagner, Solar Physics  
Branch, Space Physics Division, Code SS, NASA Headquarters, Washington, D.C. 20546



**STUDY OF MAGNETIC STRUCTURE IN  
THE SOLAR PHOTOSPHERE AND CHROMOSPHERE**  
**Final Report, Grant NAGW-2545, June 1 1991 through  
September 30 1997**

Principal Investigator, Robert W. Noyes  
Co-Investigators: Eugene Avrett, Peter Nisenson, Han Uitenbroek,  
Adriaan A. van Ballegoijen

**1. Introduction**

This grant funded an observational and theoretical program to study the structure and dynamics of the solar photosphere and low chromosphere, and the spectral signatures that result. The overall goal is to learn about mechanisms that cause heating of the overlying atmosphere, and produce variability of solar emission in spectral regions important for astrophysics and space physics. The program exploited two new ground-based observational capabilities: one using the Swedish Solar Telescope on La Palma for very high angular resolution observations of the photospheric intensity field (granulation) and proxies of the magnetic field (G-band images); and the other using the Near Infrared Magnetograph at the McMath-Pierce Solar Facility to map the spatial variation and dynamic behavior of the solar temperature minimum region using infrared CO lines. We have interpreted these data using a variety of theoretical and modelling approaches, some developed especially for this project.

Previous annual reports cover the work done up to 31 May 1997. This final report summarizes our work for the entire period, including the period of no-cost extension from 1 June 1997 through September 30 1997. In Section 2 we discuss observations and modelling of the photospheric flowfields and their consequences for heating of the overlying atmosphere, and in Section 3 we discuss imaging spectroscopy of the CO lines at  $4.67 \mu$ .

**2. Dynamics of Flowfields and Magnetic Flux Elements  
in the Solar Photosphere**

We studied the interaction of photospheric magnetic fields and convection using a time series of high resolution G-band and continuum filtergrams obtained at the Swedish Vacuum Solar Telescope (SVST) at La Palma by the Lockheed group (van Ballegoijen et

al 1998). The purpose of this study was to obtain a better understanding of the motions of magnetic elements in the photosphere and the likely effect of these motions in terms of heating the upper atmosphere. The solar chromosphere and corona are generally believed to be heated by MHD waves or other disturbances which propagate upward along magnetic flux tubes from the convection zone. Our goal is to detect these tranverse motions in flux tubes at the photospheric level, and thereby put observational constraints of the amount of energy injected into the upper atmosphere. Therefore, while we did not analyze coronal observations in this study, the results reported here are nevertheless relevant to the problem of coronal heating.

## 2.1. Background to the Problem

Observations of the Sun with high spatial resolution show network bright points (Muller 1983, 1985, 1994; Muller & Keil 1983; Muller & Roudier 1984, 1992) and “filigree” (Dunn & Zirker 1973; Mehlretter 1974; Berger et al. 1995), which are small bright features located within the intergranular lanes. The bright points and filigree are seen in the wings of strong spectral lines such as  $H\alpha$  and Ca II H & K, in lines formed in the photosphere, and even at continuum wavelengths (with reduced contrast). The widths of these structures is 100 to 200 km, at the limit of resolution of ground-based solar telescopes. The bright points are associated with regions of strong magnetic field (Chapman & Sheeley 1968; Title, Tarbell & Topka 1987; Simon et al. 1988; Title et al. 1989, 1992; Keller 1992) and correspond to magnetic flux tubes of kilogauss field strength that stand nearly vertically in the solar atmosphere (Stenflo 1973; Stenflo & Harvey 1985; Sanchez Almeida & Martinez Pillet 1994; see review by Solanki 1993). The filigree produce abnormal granulation patterns (Dunn & Zirker 1973) and appear to be chains of bright points which fill the intergranular lanes.

The dynamical behaviour of bright points has been studied by many authors. Muller (1983) found that facular points on the quiet sun are predominantly located in patches at the periphery of supergranule cells, indicating that the magnetic elements are advected by the supergranular flow. Muller et al. (1994) measured velocities of 29 isolated bright points and found a mean speed of 1.4 km/s. Strous (1994) studied bright points in a growing active region; using line-center images taken in Fe I 5576 Å, he found velocities between 0.26 km/s and 0.62 km/s. Berger & Title (1996) measured velocities of 1 to 5 km/s for G-band bright points in the “moat” around a sunspot; they showed that the motions are constrained to the intergranular lanes and are primarily driven by the evolution of the granulation pattern. They found that the bright points continually split and merge, with a mean time between splitting events of few hundred seconds. Berger et al. (1998) observed

a similar rapid splitting and merging of bright points in an enhanced network region.

## 2.2. Vorticity and Divergence in the Solar Photosphere

Our initial efforts to trace motions of bright points in the photosphere utilized an excellent series of photospheric observations obtained from Pic du Midi observatory, supplemented by observations from the Swedish Solar Telescope at La Palma to measure the vorticity and divergence of flows in the photosphere. As magnetic flux knots collect in regions of converging flow at the vertices of mesogranules and supergranules, conservation of momentum should lead to a significant vorticity in the flow. Contrariwise, for diverging flow (e.g. outflow from a local source of upwelling material) conservation of angular momentum should cause the vorticity to decrease. We calculated the horizontal vector flow field using a correlation tracking algorithm, and from this derived three scalar fields: the horizontal flow speed, the divergence of the flow, and the vertical component of the curl of the flow. We found that the divergence of the flow has more power and greater lifetime than does the curl; that is, episodes of inflow or outflow are longer-lived and greater in amplitude than episodes of significant curl or vorticity. The largest values of divergence are statistically found in regions where the horizontal flow speed is largest; we associate these regions with exploding granules. Regarding the relation between vorticity and divergence, as predicted the highest vorticity is statistically associated with areas of negative divergence, i.e. with converging flow, such as intergranular lanes or vertices of granular, mesogranular, and supergranular flow. The effect is not large, but statistically significant. A study of the flowfields in a numerical simulation of convection showed a similar dependence of vorticity on divergence, so this would seem to be a general property of convection.

The above conclusions resulted from a statistical analysis. We also sought examples where we could see visual evidence of strong vorticity in the granulation flow. Somewhat to our surprise, only rarely did we find events with vorticity strong enough to dominate the random component of the turbulent flow; one such event however had a remarkably large circulation velocity, of 3 km/s around a radius of 450 km; this corresponds to one rotation every 1000 seconds.

This research was carried out and published together with Harvard undergraduate student Wang Yi (Wang et al 1995).

### 2.3. Tracking of Bright Points Using G-Band Data

In our more recent study we use the observational data of Löfdahl (1996) to study the proper motions of bright points and their interactions with the granulation flow. The data were obtained at the SVST on La Palma on 1995 October 5 between 10:57 and 12:08 UT, and were kindly provided to us by the Lockheed group. The field-of-view (FOV) is a 29 by 29 arcsec area near solar disk center containing an enhanced network region. Observations were made simultaneously with two CCD cameras, one with a filter centered at a wavelength of 4305 Å (the so-called G band which contains absorption lines due to the molecule CH), the other with a filter centered at a wavelength in the continuum (4686 Å). Frame selection was based on the G band images: only the three best frames in each 20-second evaluation period were retained for analysis. Both cameras were equipped with phase-diversity beam splitters which put two images on each CCD with a difference in focus position. The images were corrected for seeing effects using Partitioned Phase-Diverse Speckle restoration, and were carefully coaligned using image destretching techniques. The data were space-time filtered to remove the effects of solar p-mode oscillations. The result is a time series of 180 images with very high spatial resolution covering a period of about 70 min. The image scale is 0.083 arcsec/pixel and the mean time between frames is 23.5 s. For a detailed description of the observation and image restoration procedures, see Löfdahl et al (1998) and Berger et al (1998).

The G-band images show both the bright points and the solar granulation pattern. To isolate the bright points, we construct “magnetic” difference images by subtracting G-band and continuum images,  $I_{magn} = I_{4305} - I_{4686}$ , where  $I_{4305}$  and  $I_{4686}$  are intensities normalized to the mean intensity in the non-magnetic areas. Examples of such difference images are shown in Figures 1a and 1b (frames 40 and 177 of the time sequence). We measured the motions of bright points using an object tracking technique applied to such difference images.

One difficulty in tracking bright “points” is that they are often not point-like at all but have complex linear shapes, so that their positions are not well defined. Therefore, we developed a new tracking method which uses small but finite-size, non-overlapping “corks”, i.e., small circular disks (radius  $r_0 = 60$  km) which can move about on the plane of the photosphere but cannot overlap each other. Each bright feature in the magnetic difference image is associated with a cluster of such corks; the total number of corks over the entire image is 1400. The corks are advected by an artificial flow field  $\mathbf{v}(x, y, t)$  which drives the corks to the brightest regions in the magnetic image (flow velocity is assumed to be proportional to the intensity gradient,  $\mathbf{v} \propto \nabla I_{magn}$ ). Clusters of corks collect at the bright regions in the image, and follow these regions as the brightness pattern evolves. To

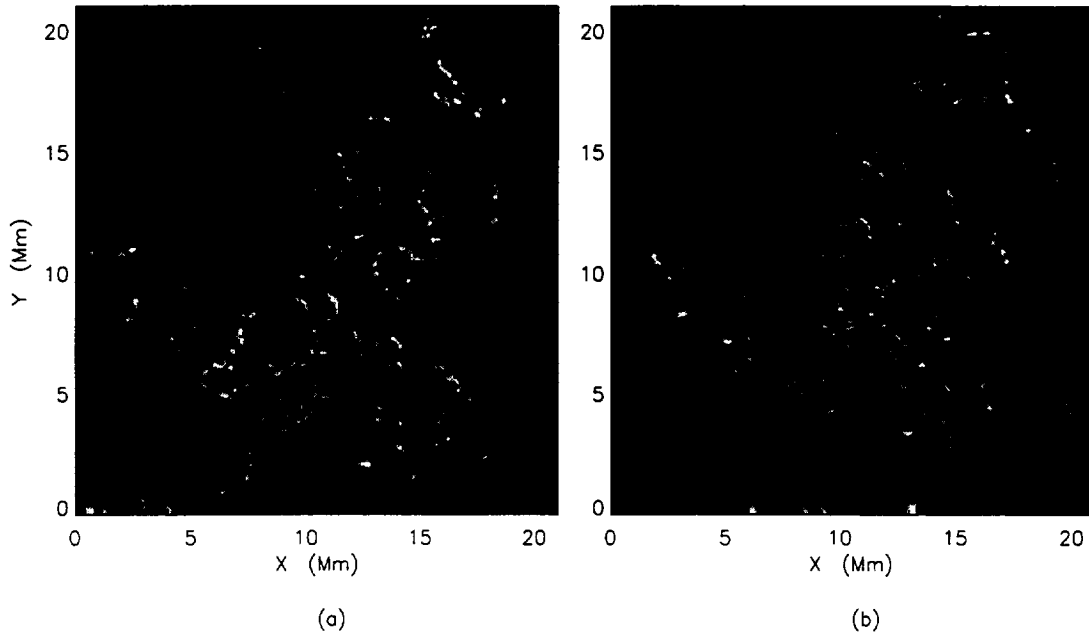


Fig. 1.— Difference images obtained by subtracting G-band and continuum images for (a) frame 40 and (b) frame 177 of the time sequence. Based on observations obtained at the Swedish Vacuum Solar Telescope at La Palma on 1995 October 5 by the Lockheed group (see Löfdahl et al 1998).

account for intensity variations of the bright points, we periodically remove corks which fall in low-intensity regions, and reinsert them in high-intensity regions. The advantage of this method is that the shapes of the cork clusters can adjust themselves to the actual shape of the bright points.

Figures 2a and 2b show the spatial distributions of corks for frames 40 and 177 plotted over the corresponding granulation intensity image. Note that the corks are located in the intergranular lanes. Comparison with Figures 1a and 1b shows that the spatial distribution of the corks closely resembles the distribution of the bright points. Therefore, we can now use the positions of the corks,  $x_k(t)$  and  $y_k(t)$ , as tracers of the bright points. This avoids having to measure the “center of gravity” of the bright points, which is very difficult in practice.

We derived the autocorrelations of the bright point velocity, i.e., the functions  $\langle v_x(t)v_x(t + \tau) \rangle$  and  $\langle v_y(t)v_y(t + \tau) \rangle$ , where  $\tau$  is the time delay, and  $\langle \dots \rangle$  denotes an average over all corks and over time  $t$ . The measured autocorrelations are plotted as

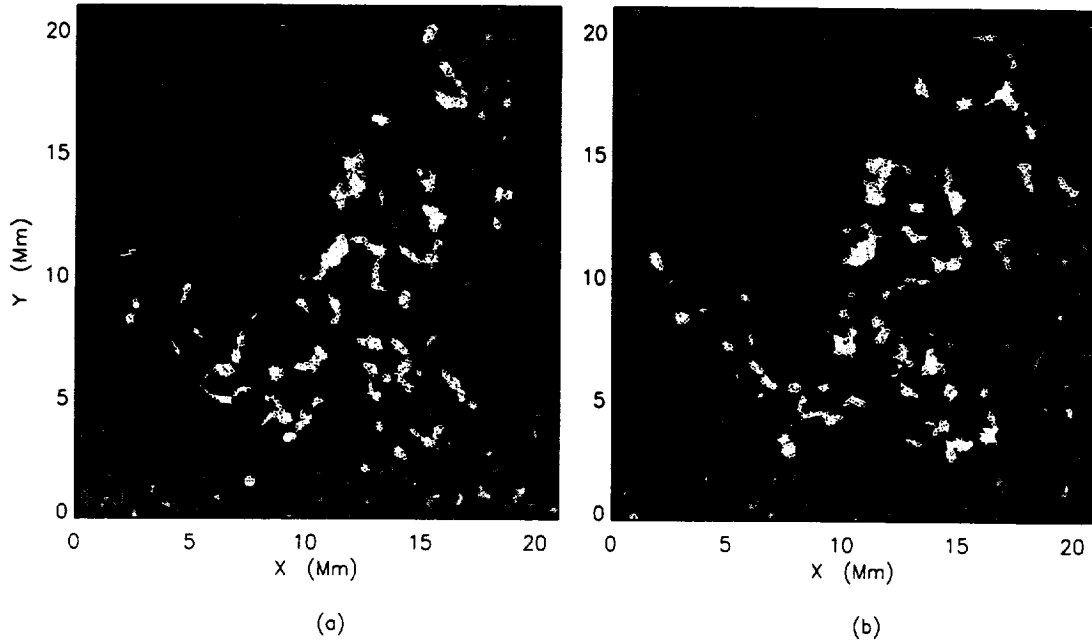


Fig. 2.— Tracking bright points with finite-size corks: (a) frame 40; (b) frame 177. The image shows the intensity granulation pattern. Note that the bright points are located in the intergranular lanes.

symbols in Fig. 3. Note that the autocorrelations decrease monotonically with increasing time delay  $\tau$ , i.e., there is no evidence for any specific periodicities in the bright point motion. The rapid decrease seen for short time delays (less than 3 frames) is attributed to the noise in the measurement of bright point positions, but the more gradual decrease on a time scale of a few hundred seconds is probably real. We find that the data can be fit by a Lorentzian function with a half-width  $\tau_0 = 100$  s and an amplitude of  $0.12 \text{ km}^2\text{s}^{-2}$ , superposed on a constant background ( $0.01 \text{ km}^2\text{s}^{-2}$ ). Therefore, the bright points exhibit random motions with a correlation time of about 100 seconds. These random motions are due to buffeting by the granulation flow.

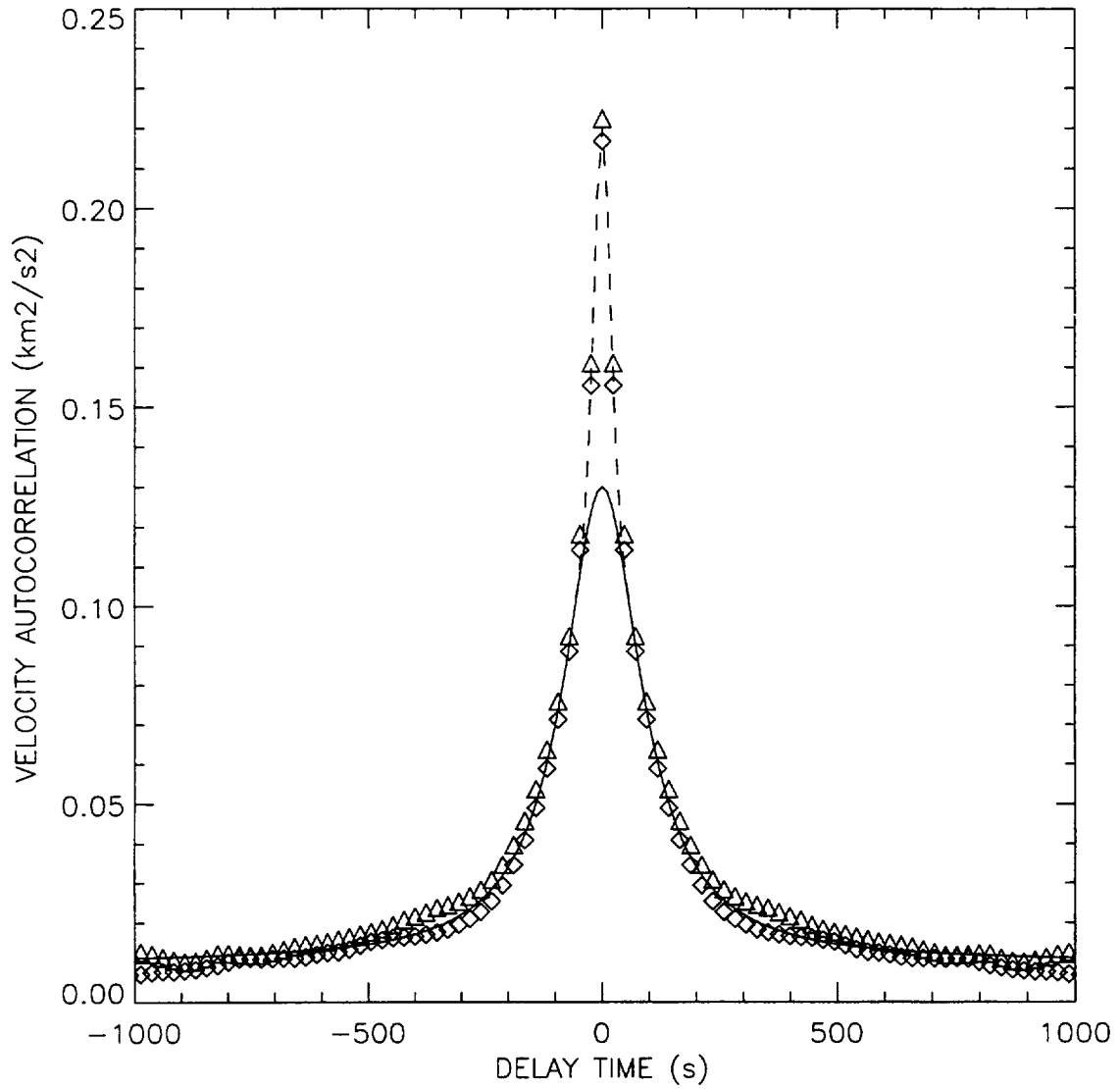


Fig. 3.— Autocorrelations of the measured bright point velocity:  $\diamond$  for  $\langle v_x(t)v_x(t + \tau) \rangle$ ;  $\triangle$  for  $\langle v_y(t)v_y(t + \tau) \rangle$ . The *full curve* is a Lorentzian fit to the data for time delays of at least 3 frames (70 s). The *dashed curve* indicates the contribution attributed to measurement noise.

## 2.4. Simulation of Granulation Flow and Flux Tube Motion

To understand the processes that determine the spatial distribution of the bright points, we constructed time-dependent models of the granulation flow and simulated the motions of magnetic flux elements in response to this flow. The granulation flow models are derived from the *observed* granulation pattern, using a simple 2D hydrodynamic model that includes horizontal temperature gradients and the inertia of the horizontal flow. The model is based on the assumption that the vertical vorticity of the flow is small, so that the velocity can be approximated as  $\mathbf{v} = -\nabla\phi$ , where  $\phi(x, y, t)$  is the flow potential. We assume that the acceleration of the plasma is given by:

$$\frac{\partial \mathbf{v}}{\partial t} + \mathbf{v} \cdot \nabla \mathbf{v} = -c_1 \nabla I_{conv} + \nu \nabla^2 \mathbf{v} - \frac{\mathbf{v}}{\tau_f}, \quad (1)$$

where  $I_{conv}(x, y, t)$  is the observed intensity pattern, the second term describes the effects of turbulent viscosity ( $\nu = 70 \text{ km}^2/\text{s}$ ), and the third “frictional” term describes the decay of the granule velocity after the granule has disappeared from the temperature field (decay time  $\tau_f = 300 \text{ s}$ ). The proportionality constant  $c_1$  is determined by comparing the computed flow velocities with those found in the 3D granulation simulations of Stein & Nordlund (1994). At a depth of 40 km in Stein & Nordlund’s model the irrotational component of horizontal velocity (i.e., after removal of vortical flows) has an rms value  $v_{x,rms} \approx v_{y,rms} \approx 1.60 \text{ km/s}$ . We adjusted  $c_1$  to obtain essentially the same rms velocity in the present model.

Fig. 4a shows the divergence of the velocity for frame 40 of the time sequence, as derived from our simple 2D model. For comparison, Fig. 4b shows the divergence of the horizontal component of velocity at a depth of 40 km in Stein & Nordlund’s (1994) model. Note that the intergranular lanes are very narrow in both cases ( $\sim 100 \text{ km}$ ).

We use our simulated flow fields to predict the horizontal motions of magnetic elements in the observed region of the photosphere. The magnetic field is modeled as a collection of cylindrical flux tubes which stand vertically in the solar atmosphere and each have a radius  $r_0 = 60 \text{ km}$ . Each flux tube is a rigid structure which is *passively advected* by the granulation flow, i.e., we neglect possible effects of the anchoring of the flux tubes at larger depth. The rigidity of the flux tubes simulates the fact that the magnetic field strength  $B$  cannot exceed the value for equipartition of the magnetic pressure with the external gas pressure in the lower photosphere. Assuming  $B = 1500 \text{ G}$  and  $r_0 = 60 \text{ km}$ , each flux tube has a magnetic flux of  $1.7 \times 10^{17} \text{ Mx}$ . The flux tubes behave like rigid “corks” which float on the granulation flow: converging flows produce densely packed cork clusters which represent larger magnetic elements with shapes determined by the flow. The motions of 1400 corks are followed from frame 3 to frame 177, which corresponds to about 7 granulation lifetimes.

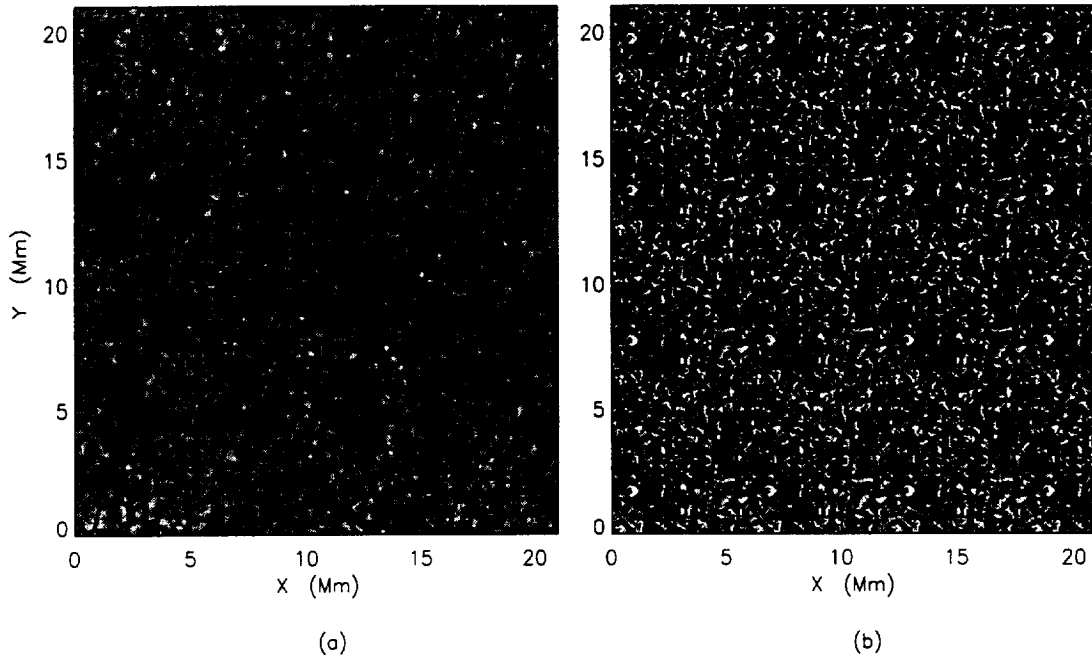


Fig. 4.— Divergence of granulation flow velocity: (a) as computed for frame 40 of the La Palma data using the 2D model presented in §2.4; (b) as derived from 3D simulations of solar granulation by Stein & Nordlund (1994), displayed on the same the spatial scale and resolution as the La Palma data set.

The initial positions of the corks are chosen to coincide with the positions of the bright points.

Figure 5 shows the cork positions for frames 40 and 177 superposed on the corresponding convective intensity patterns. Note that the corks occur in clusters located at the vertices where several intergranular lanes intersect. Linear structures extend from these clusters out into the intergranular lanes; this is due to the narrow width of the velocity lanes, which prevents the corks from all collecting at the vertex points. Although the present model does not reproduce the exact locations of all bright points in the final frame, the qualitative agreement between observed and predicted patterns is quite good (compare Figures 2 and 5). In particular, the model shows linear structures similar to the observed filigree. In contrast, in models with broader lanes most of the magnetic elements collect in a few large clusters, in disagreement with the observed bright point pattern. We conclude that the small width of the intergranular lanes plays an important role in the dynamics of the photospheric magnetic field. The fact that the passive advection model works so well

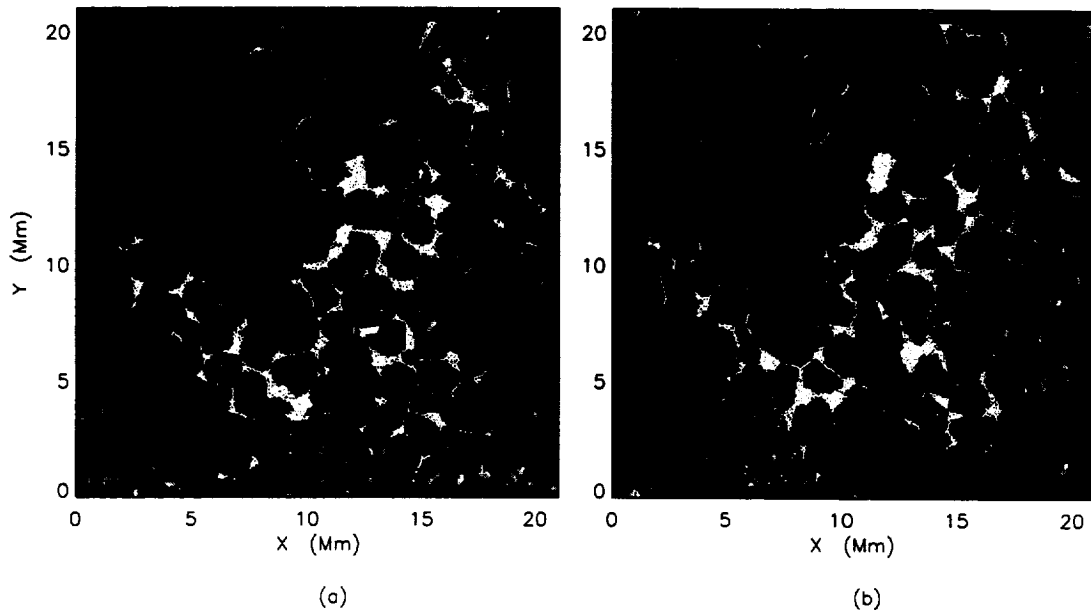


Fig. 5.— Results from a simulation of the motions of photospheric magnetic flux elements: (a) frame 40, (b) frame 177. The assumed granulation flow field was derived from the observed intensity pattern.

suggests that the flux tubes are not strongly affected by their anchoring at large depth, at least not on a time scale of about 1 hour.

## 2.5. Potential-Field Modeling

The magnetic flux tubes on the Sun fan out with height, and above some height the neighboring flux tubes merge to fill the available volume. This “merging” of the flux tubes generally occurs in the chromosphere at a height of about 1000 km or less (depending on the horizontal distance between the flux tubes). Since the magnetic field is nearly “frozen into” the plasma, the horizontal motions of the photospheric flux tubes induce plasma flows in the chromosphere and above. One expects transverse MHD waves to be excited in the flux tubes by granular buffeting and sudden footpoint motions, and these waves may grow to considerable amplitude in the chromosphere.

In this section we use potential-field modeling to compute the velocity of the field lines in a quasi-statically evolving field configuration, i.e., we neglect the effects of the MHD

waves. Since it is difficult to track the field lines, a massless ideal plasma is introduced which allows us to use the MHD equations to compute the velocity field. The model assumes that the magnetic field inside the flux tubes can be approximated as a potential field from discrete point sources:

$$\mathbf{B}(\mathbf{r}, t) = \sum_k \mathbf{B}_k(\mathbf{r}, t). \quad (2)$$

The sources are located at depth  $d_0 = 160$  km below the photosphere, and their horizontal coordinates  $x_k(t)$  and  $y_k(t)$  are functions of time. Each source is the sum of a monopole and a (vertically oriented) dipole, and we assume that all sources have the same strength and polarity. We define tube-like structures by tracing magnetic field lines downward from a height of 1500 km in the chromosphere. The frozen-in condition implies  $\mathbf{E} + \mathbf{v} \times \mathbf{B} = 0$ , where  $\mathbf{v}(\mathbf{r}, t)$  is the plasma velocity and  $\mathbf{E}(\mathbf{r}, t)$  is the electric field. The latter consists of an inductive part and an electrostatic part:

$$\mathbf{E}(\mathbf{r}, t) = \sum_k \mathbf{E}_k(\mathbf{r}, t) - \nabla\Phi, \quad (3)$$

where  $\Phi(\mathbf{r}, t)$  is the electric potential, and  $\mathbf{E}_k(\mathbf{r}, t)$  is the induction electric field from a single source:

$$\mathbf{E}_k(\mathbf{r}, t) \equiv -\mathbf{v}_k(t) \times \mathbf{B}_k(\mathbf{r}, t). \quad (4)$$

Here  $\mathbf{v}_k(t) \equiv d\mathbf{r}_k/dt$  the source velocity. The frozen-in condition implies  $\mathbf{E} \cdot \mathbf{B} = 0$ , which yields:

$$\mathbf{B} \cdot \nabla\Phi = \sum_k \mathbf{B} \cdot \mathbf{E}_k. \quad (5)$$

Note that the right hand side can be computed directly from the known positions and velocities of the magnetic sources, hence the electric potential  $\Phi(x, y, h_0, t)$  at height  $h_0 = 1500$  km can be determined by numerical integration along the magnetic field lines (we use the boundary condition that  $\Phi(x, y, 0, t) = 0$ ). This yields the electric field, from which we can compute the velocity using  $\mathbf{v} = \mathbf{E} \times \mathbf{B}/B^2$ . Here we assumed that the velocity is perpendicular to the magnetic field lines.

We use the above method to predict the magnetic and velocity fields above the observed network region. The positions of the magnetic sources are taken from the simulation described in §2.4. Figure 6 shows a perspective view of field lines for a small area in frame 40. The horizontal size of the region is 3000 km, and its location within frame 40 is indicated by the white box in Figure 5a. Figure 7a shows the horizontal component of velocity in the chromosphere (height  $h_0 = 1500$  km) as computed with the above method. Figure 7b shows the boundaries between different flux tubes at this height, i.e., each domain is connected to one particular ‘‘cork’’ at  $z = 0$ . Note that the predicted chromospheric velocities are

several km/s, much larger than the assumed velocities of the magnetic sources below the photosphere. This amplification is due to two effects: (1) The spreading of the flux tubes with height enhances the rotational motion of neighboring flux tubes around each other. (2) The velocity is further enhanced close to the *separatrix surfaces* where neighboring flux tubes slide rapidly past each other. The latter effect is due to the existence of magnetic nulls in these magnetic configurations. The velocity enhancement predicted by this model are so large that the inertia of the gas can no longer be neglected in the vicinity of the separatrices. Clearly, to obtain an accurate description of such flows more realistic MHD models of interacting flux tubes are needed.

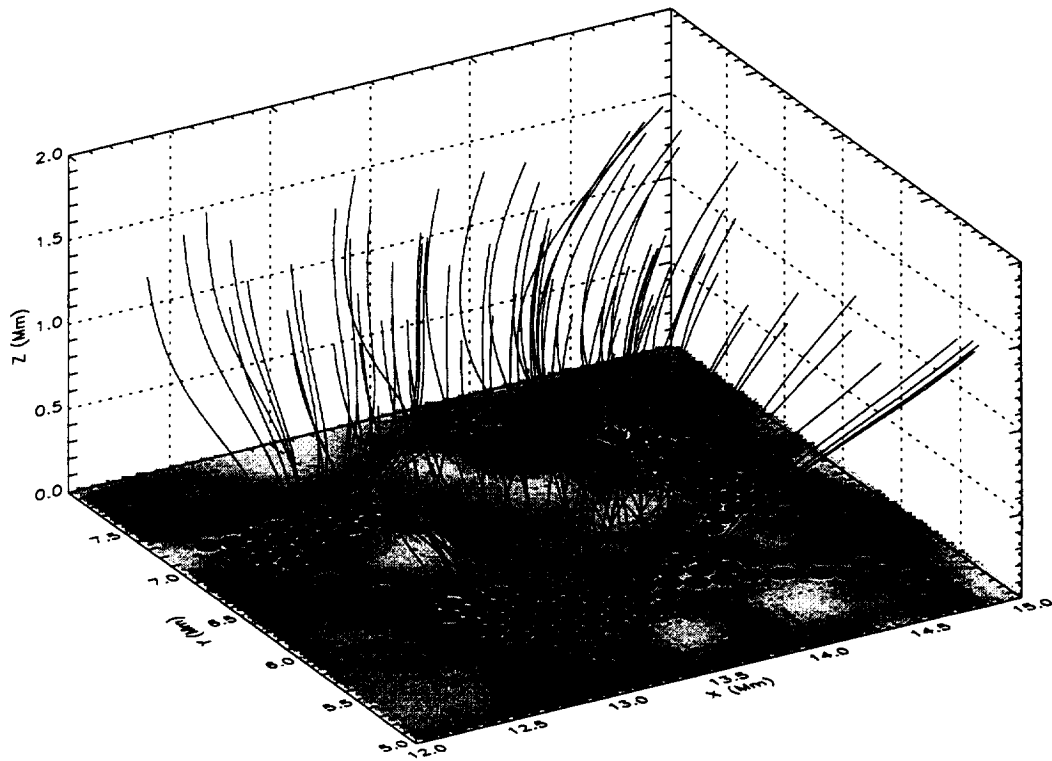


Fig. 6.— Potential-field model of magnetic flux tubes in the solar atmosphere. The model corresponds to a small region in frame 40 of the La Palma data set (indicated by the white box in Fig. 5a).

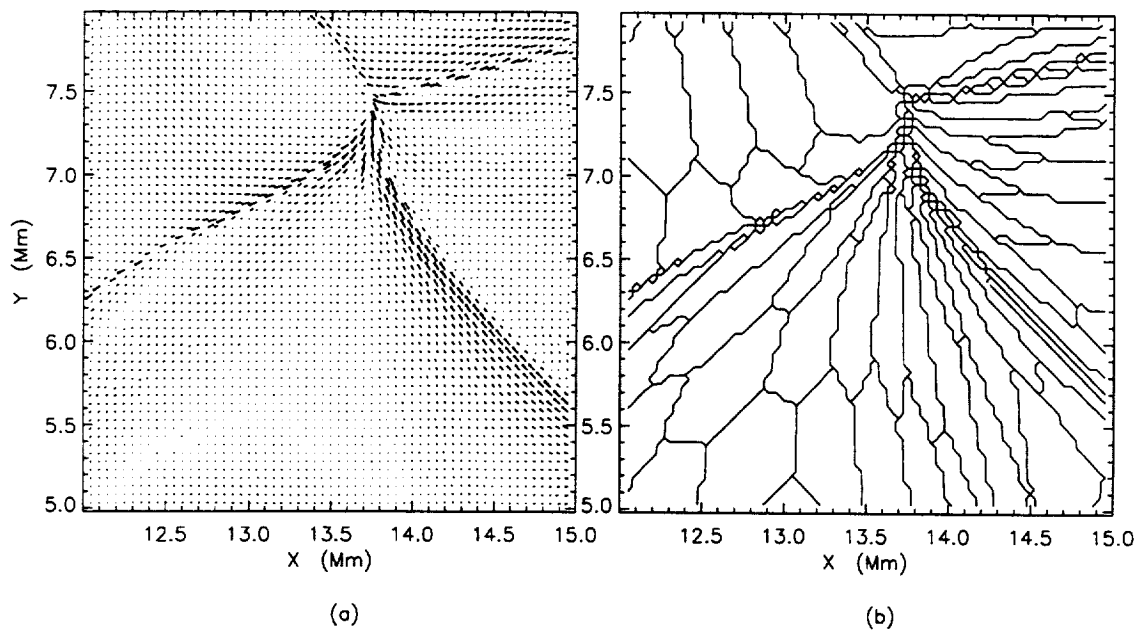


Fig. 7.— (a) Horizontal velocity at a height of 1500 km in the chromosphere as predicted from the potential-field model for the region shown in Fig. 6. The longest arrows in this plot correspond to 5 km/s, and the bold arrows show the direction of the field in regions where the horizontal velocity exceeds 5 km/s. (b) Separatrices between different flux tubes.

## 2.6. Development of Image Reconstruction Algorithms

Blind Iterative Deconvolution (BID) is a technique which can correct the degrading effects of atmospheric turbulence on astronomical images from single short exposure, high signal-to-noise-ratio frames (see, for example, Christou et al 1995; Jeffries et al 1993; Restaino 1992). At the Center for Astrophysics, we have implemented a version of BID following the general approach of (Ayers & Dainty 1988), but extending the technique to use Wiener filtering (Nisenson 1991) and by implementing a special version for solar imaging. BID searches for the point spread function (psf) and deconvolved image which, when convolved with each other, best match the input data. The process first deconvolves the data with a first guess of the psf (usually a gaussian having a diameter which roughly matches the “seeing” for the data frame). This deconvolved image is then used in a second deconvolution of the data to find a new estimate of the psf. After each operation, image plane and Fourier plane constraints are applied (e.g. positivity, image support, low-pass filtering, etc). When a stable solution is reached, the iteration is halted. While this process has not been proven to have unique solutions, it appears that with proper constraints that the results accurately recover the psf and deconvolved image.

High resolution imaging of solar features is an ideal application for BID, since the rapid evolution of solar granulation does not allow recording of the long sequences of speckle frames needed for convergence of more standard speckle techniques. Also, the signal-to-noise ratio is normally very high, a necessary condition for BID. Two major problems are encountered in applying BID to solar frames. First, the atmospheric isoplanatic patch is typically only a few arcseconds in size, even for good seeing conditions, so reconstructions covering an extended area must be carried out on small, overlapping fields and then spliced together into a larger field. The other problem is that each of these small fields has bright structure extending right to the boundary of the field. Edge to edge intensity gradients can introduce severe edge effects in the form of high contrast ringing which extends well into the frame. This is not a problem for stellar images, where the surrounding field is dark, and edge effects are negligible. Direct application of BID to raw solar images produces strong edge effects and ringing which appear to propagate over almost the whole field. This effect is particularly degrading if there are large intensity gradients across the image. The key to eliminating (or nearly eliminating) the ringing is to remove the edge to edge intensity differences in the original frames. To do this, we implement a technique called detrending.

In detrending, we first produce a version of the input image which has only the lowest frequencies in it by using low-pass Fourier plane filtering. The range of frequencies in this image is set so that only features which are well resolved by the atmospheric blurring remain. This low-pass image is then subtracted from the original image, and the remainder

of this subtraction, containing only high frequencies, is then used in the BID restoration process. In addition, a Gaussian rolloff is applied to the borders of the detrended image, further reducing any remaining edge effects. We use a somewhat oversized field-of-view so that, at the end of the process, the rolled-off borders can be discarded. Finally, a retrending step is used to restore the low frequencies in the image, by adding back in the low-pass filtered version of the image. The result appears to avoid almost any measurable edge ringing, producing a sharpened version of the original image. Without detrending, the edge effects not only degrade the region near the image borders, they also dramatically affect the convergence of the process.

Figure 8 shows an example of applying BID to a G-band image taken at La Palma in 1994 with essentially the same equipment as described above for the 1995 data set we analyzed, except that no phase diversity beam splitter was used. The image on the left is the data prior to BID processing showing a region of enhanced magnetic activity with some small pores in the field. The region is a 480x480 subarea of the full frame sampled with 0.083" pixels. We partitioned this area into four 256x256 pixel subfields and processed each of them independently through the BID process. We then "stitched" them together by matching the overlap regions. The result is shown on the right. While the seeing was good in the original data, clearly the BID image is uniformly sharper and the smallest scale features are on the scale of the telescope diffraction limit (0.2").

Measurements of velocities, vorticity, and lifetimes of photospheric bright points requires that high resolution images be obtained over many hours. Since the atmosphere rarely produces such long stretches of good seeing, BID correction is crucial in providing consistent and stable image sequences.

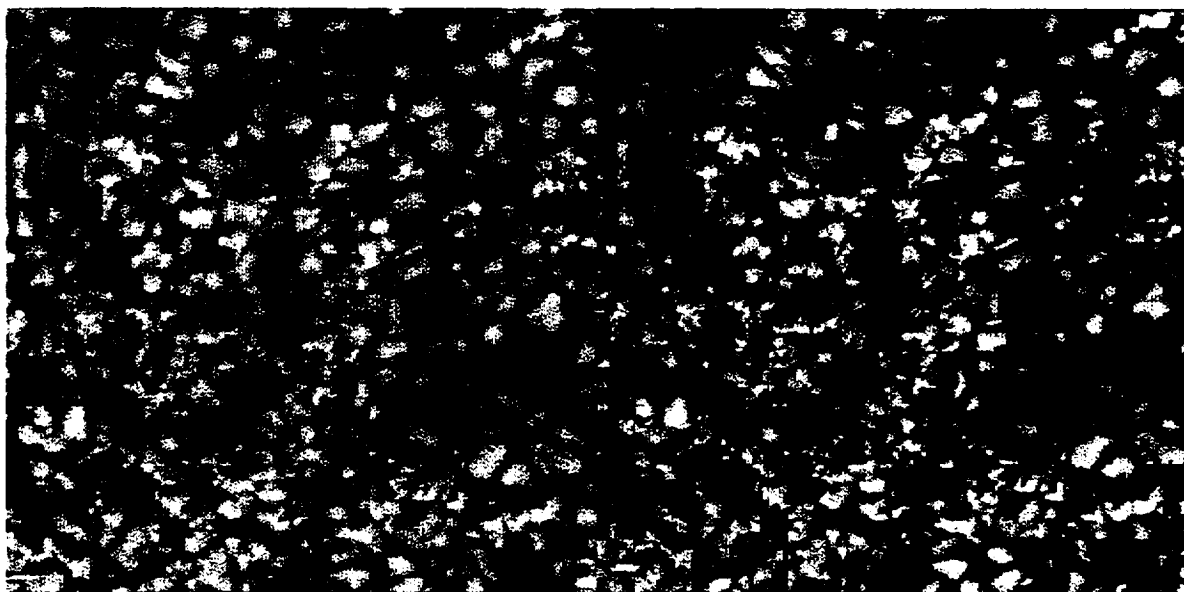


Fig. 8.— Blind Iterative Deconvolution Processing of a G-Band image. Left side is the raw image. Right side after BID processing.

### 3. Imaging Spectroscopy of the CO Rotation-Vibration Lines at $4.67 \mu$

#### 3.1. Motivation

The goal of this part of the project was to study the magnetic structure of the solar photosphere and chromosphere in order to ultimately understand where the heating of the chromosphere, transition region, and corona takes place, and where the energy for this heating comes from. We proposed to try understand how the magnetic field is embedded in the atmosphere, and where the transition occurs from a gas pressure dominated atmosphere to a magnetically dominated plasma. This requires also knowledge of the non-magnetic region, which at lower altitudes surrounds and constrains the magnetic fields, and through which part of the energy that heats the upper regions in the atmosphere flows, possibly in the form of acoustic waves generated by the convection. For this non-magnetic region the lines of the carbon-monoxide (CO) molecule form an interesting diagnostic because they do not agree with many other diagnostics that form at similar altitudes in the atmosphere.

The cores of strong vibration-rotation lines of CO show temperatures as low as 3700 K when observed near the solar limb, while other diagnostics like the UV continuum, the millimeter wavelength continuum, and the wings of strong ionic lines like Ca II H&K only show minimum temperatures of about 4000 K. However, the interpretation of observed intensities in terms of atmospheric temperatures is strongly model dependent, and clearly none of the traditional plane-parallel hydrostatic models can accommodate all diagnostics at the same time. Instead, the interpretation of solar spectra should rather be done in a manner that takes account of the inherently inhomogeneous and dynamic nature of the solar atmosphere. Thus, the CO lines should provide us information on where our traditional one-dimensional modeling of the solar photosphere and chromosphere breaks down.

#### 3.2. Strategy

To investigate where the dark CO line cores originate we have done both observations and theoretical line formation calculations of the strong fundamental rotation-vibration lines near  $4.67 \mu\text{m}$ . Figure 9 shows the spectrum at that wavelength with line identifications.

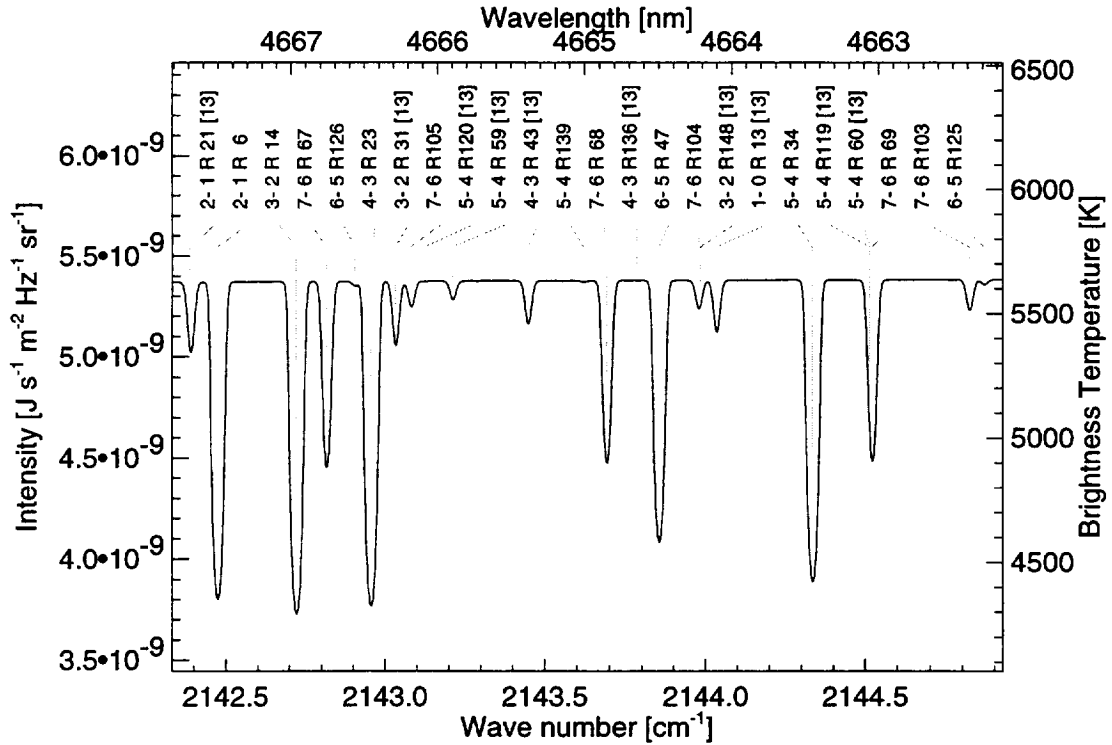


Fig. 9.— Sample spectrum of CO fundamental vibration rotation lines near  $4.67 \mu\text{m}$ . This particular spectrum was calculated for disk center from a theoretical 1-D model atmosphere that matches most CO lines but not the UV diagnostics (Avrett 1995). Lines from the  $\text{C}^{13}\text{O}^{16}$  isotope are marked with [13].

### 3.2.1. Theoretical line formation calculations

Much of what we know about the solar granulation has been learned from hydrodynamical simulations, which show remarkable agreement with observed granulation patterns at continuum wavelengths (e.g. Stein & Nordlund 1998), while they make detailed predictions of convective flows below the visible surface. These simulations provide, therefore, a physical model to study CO line formation in a (non-magnetic) inhomogeneous atmosphere.

Radiative transfer calculations were done of CO line formation in a three-dimensional snapshot of a hydrodynamic solar granulation simulation by Stein & Nordlund (1989). Although the line source function of the CO lines themselves was assumed to have LTE

values, the total source function of line plus continuum was not a priori required to do so. A full three-dimensional transfer solution was obtained of the radiation field with a newly developed transfer code. The molecules, which included all species relevant for the solar atmosphere like  $\text{H}_2$ ,  $\text{H}_2^+$ ,  $\text{HC}$ ,  $\text{HO}$ ,  $\text{HN}$ ,  $\text{H}_2\text{O}$ ,  $\text{CO}$ ,  $\text{CN}$ ,  $\text{C}_2$ ,  $\text{O}_2$ , and  $\text{N}_2$ , were assumed to be in chemical equilibrium, i.e., no time-dependent chemical evolution was considered.

### 3.2.2. *Observations at Kitt Peak*

Spatially and temporally resolved long-slit spectra of a number of CO fundamental vibration-rotation lines at  $4.67 \mu\text{m}$  were obtained with the Near Infrared Magnetograph (NIM) at the 1.5 m McMath-Pierce facility of the National Solar Observatory at Kitt Peak. The infrared spectrograph (with a theoretical resolution of 90 000) was used to project long-slit spectra onto a  $256 \times 256$  InSb detector. Spectra could be obtained with a minimum 2 sec cadence, during which the slit was either stepped over the solar surface to produce a spectro-heliogram, or kept at a fixed location for a time-sequence of one single slit position. The data cubes obtained in this way could be used to produce maps (in either  $x$ - $y$  or  $x$ - $t$ ) of any function of wavelength on the detector. In particular, maps were produced of the CO line-core brightness, which serves as a proxy for temperature, CO line-core shift, which is a proxy for line-of-sight velocity, and line width.

Flat fielding the CO spectra is a difficult task because there is no spectrally flat light source available at the telescope at  $4.67 \mu\text{m}$ . There are two options to work around this: (1) Move the telescope and diffraction grating while adding up exposures to average out spatial and spectral features; this works well for the spatial direction since the contrast is low in the infrared, but spectral lines are more difficult to remove. (2) Use a theoretical spectrum (like the one in Figure 9) broadened by the instrumental profile to prescribe what the shape of the spatially averaged observed spectrum should be (see Ayres & Rabin 1996). We used mostly the second method because it does not rely on the difficult to control quality of the spatially and spectrally averaged flat fields. Where possible results with both methods were compared and found to agree well.

## 3.3. Results

### 3.3.1. *Theoretical line formation calculations*

As an example of our theoretical CO calculations the two panels of Figure 10 show the intensities in the core of the CO 7–6 R68 (right panel) and the neighboring continuum (left

panel) computed from the 3-D snapshot. Note that the centers of granules appear dark and the inter-granular lanes appear bright in the core of the CO line. Such a reversal of

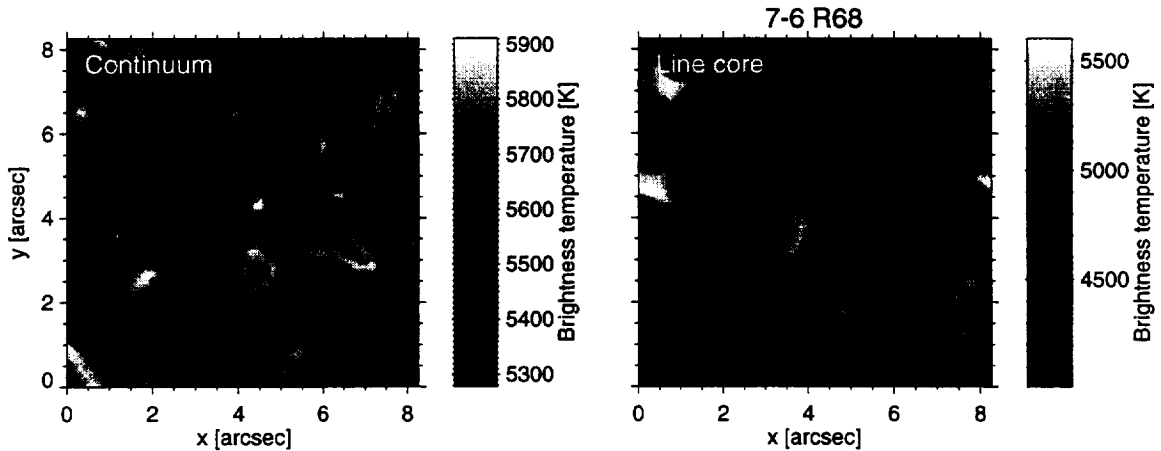


Fig. 10.— Disk-center brightness temperatures in the CO 7–6 R68 line (right panel) and neighboring continuum (left panel) calculated from a theoretical granulation model.

contrast compared to the continuum is also observed in the wings of the Ca II H&K lines (Evans & Catalano 1972). The granules appear dark in the CO line because of the strong adiabatic expansion cooling that occurs when the upflowing granule runs into the steep density gradient of the photosphere. When the divergent flow is compressed again over the inter-granular lanes, where the downflows occur, it is heated by compression and appears bright in the CO line.

### 3.3.2. Observations at Kitt Peak

As examples of our Kitt Peak observations we present a spectro-heliogram in the core of the CO 3–2 R14 line and a time-series of spectra with fixed slit position. The spectro-heliogram in Figure 11 was constructed by scanning the spectrograph slit over the solar surface in  $0''.5$  steps, taking a long-slit spectrum in each position. The  $x$ -axis is parallel to the slit, the  $y$ -axis is in the direction of the scanning motion, parallel to the dispersion. In each exposure the intensity in the core of the strong CO 3–2 R14 line (see Figure 9) was measured and converted to the equivalent brightness temperatures imaged here. During the accumulation of this heliogram on 6 May 1994 seeing conditions were exceptionally good, so that the spatial resolution is close to the theoretical limit which is  $0''.8$  for the 1.5 m primary at  $4.67 \mu\text{m}$ .

#### 4. Papers Published with Support of this Grant

Imaging Spectroscopy of the Solar CO Lines at  $4.67 \mu\text{m}$ . Uitenbroek, H., Noyes, R.W., and Rabin, D. 1994, ApJ, 432, L67-70.

New Insight in the Solar Tmin Region from the CO Lines at  $4.67 \mu\text{m}$ . Uitenbroek, H., and Noyes, R.W. 1994, in *Chromospheric Dynamics*, Proc. OSLO mini-workshop June 1994 (Mats Carlsson, ed.), 129-138.

Two-component Modeling of the Solar IR CO Lines. Avrett, E.H. 1995, Proceedings 15th NSO/Sacramento Peak Workshop, *Infrared Tools for Solar Astrophysics: What's Next?*

Vorticity and Divergence in the Solar Photosphere. Wang, Y., Noyes, R.W., Tarbell, T.D., and Title, A.M. 1995, ApJ, 447, 419-27.

Modeling of Temporal Variations in the Solar Chromosphere. Avrett, E.H., Höflich, P., Uitenbroek, H. 1996, in R. Pallavicini and A.K. Dupree (eds.), *Cool Stars, Stellar Systems, and the Sun*, Ninth Cambridge Workshop, PASP Conference Series Vol. 109, p. 105

The Solar Mg II h&k Lines. Observations and Radiative Transfer Modeling. Uitenbroek, H. 1997, Sol. Phys., 172, 109

The Effect of Photospheric Granulation on the Determination of the Lithium Abundance in Solar-Type Stars. Uitenbroek, H. 1998, ApJ, 498, 427

Are the Dark CO Line Cores Produced by the Solar Granulation? Uitenbroek, H. 1998, poster to be presented at the AAS in San Diego, June 7-11, 1998

Dynamics of Magnetic Flux Elements in the Solar Photosphere. van Ballegoijen, A.A., Nisenson, P., Noyes, R.W., Löfdahl, M.G., Stein, R.F., Nordlund, Å, & Krishnakumar, V. 1998, ApJ, submitted

- Ayres, T.R., & Wiedemann, G.R. 1989, ApJ, 338, 1033
- Berger, T.E., Schrijver, C.J., Shine, R.A., Tarbell, T.D., Title, A.M., & Scharmer, G. 1995, ApJ, 454, 531
- Berger, T.E., & Title, A.M. 1996, ApJ, 463, 365
- Berger, T.E., Löfdahl, M.G., Shine, R.A., & Title, A.M. 1998, ApJ, 495, in press
- Chapman, G.A., & Sheeley, N.R., Jr. 1968, Sol. Phys., 5, 443
- Christou, J.C., Hege, E.K., & Jeffries, S.M. 1995, Proc. SPIE, 2566, p. 134
- Dunn, R.B., & Zirker, J.B. 1973, Sol. Phys., 33, 281
- Evans, J.W., & Catalano, C.P. 1972, Sol. Phys., 27, 299
- Jeffries, S.M., & Christou, J.C. 1993, ApJ, 415, p. 862
- Keller, C.U. 1992, Nature 359, 307
- Löfdahl, M.G. 1996, PhD thesis, Stockholm University
- Löfdahl, M.G., Berger, T.E., Shine, R.A., & Title, A.M. 1998, ApJ, 495, in press
- Mehltretter, J.P. 1974, Sol. Phys., 38, 43
- Muller, R. 1983, Sol. Phys., 85, 113
- Muller, R. 1985, Sol. Phys., 100, 237
- Muller, R. 1994, in *R.J. Rutten & C.J. Schrijver (eds.), Solar Surface Magnetism* (Kluwer Acad. Publ.), p. 55
- Muller, R., & Keil, S. 1983, Sol. Phys., 87, 243
- Muller, R., & Roudier, Th. 1984, Sol. Phys., 94, 33
- Muller, R., & Roudier, Th. 1992, Sol. Phys., 141, 27
- Muller, R., Roudier, Th., Vigneau, J., & Auffret, H. 1994, A&A, 283, 232
- Nisenson, P. 1992, in *High Resolution in Imaging by Interferometry II*, Proc NOAO-ESO Conf, J. Beckers and F. Merkle, eds., Garching, West Germany, p. 299
- Restaino, S.R. 1992, ApOpt, 31, p. 7442
- Sánchez Almeida, J., & Martínez Pillet, V. 1994, in *M. Schüssler & W. Schmidt (eds.), Solar Magnetic Fields* (Cambridge Univ. Press), p. 316
- Simon, W.G., Title, A.M., Topka, K.P., Tarbell, T.D., Shine, R.A., Ferguson, S.H., Zirin, H., & the SOUP team. 1988, ApJ, 327, 964
- Solanki, S. 1993, Space Science Reviews, 63, 1

- Stein, R.F., & Nordlund, Å. 1989, *ApJ*, 342, L95
- Stein, R.F., & Nordlund, Å. 1994, in *D. Rabin, J. Jeffries & C. Lindsey (eds.), Infrared Solar Physics*, IAU Symp. 154 (Dordrecht: Kluwer), p. 225
- Stein, R.F., & Nordlund, Å. 1998, *ApJ*, preprint
- Stenflo, J.O. 1973, *Sol. Phys.*, 32, 41
- Stenflo, J.O., & Harvey, J.W. 1985, *Sol. Phys.*, 95, 99
- Strous, L. 1994, in *R.J. Rutten & C.J. Schrijver (eds.), Solar Surface Magnetism* (Kluwer Acad. Publ.), p. 73
- Title, A.M., Tarbell, T.D., & Topka, K.P. 1987, *ApJ*, 317, 892
- Title, A.M., Tarbell, T.D., Topka, K.P., Ferguson, S.H., & Shine, R.A. 1989, *ApJ*, 336, 475
- Title, A.M., Topka, K.P., Tarbell, T.D., Schmidt, W., Balke, C., & Scharmer, G. 1992, *ApJ*, 393, 782
- van Ballegooijen, A.A., Nisenson, P., Noyes, R.W., Löfdahl, M.G., Stein, R.F., Nordlund, Å, & Krishnakumar, V. 1998, *ApJ*, submitted
- Wang, Y., Noyes, R.W., Tarbell, T.D., Title, A.M. 1995, *ApJ*, 447, 419